ADULT NEUROGENESIS

Impact of neurodegenerative diseases on human adult hippocampal neurogenesis

J. Terreros-Roncal[1,2,3]†, E. P. Moreno-Jiménez[1,2,3]†, M. Flor-García[1,2,3]†, C. B. Rodríguez-Moreno[1,3], M. F. Trinchero[4], F. Cafini[5], A. Rábano[6], M. Llorens-Martín[1,3]*

Disrupted hippocampal performance underlies psychiatric comorbidities and cognitive impairments in patients with neurodegenerative disorders. To understand the contribution of adult hippocampal neurogenesis (AHN) to amyotrophic lateral sclerosis, Huntington's disease, Parkinson's disease, dementia with Lewy bodies, and frontotemporal dementia, we studied postmortem human samples. We found that adult-born dentate granule cells showed abnormal morphological development and changes in the expression of differentiation markers. The ratio of quiescent to proliferating hippocampal neural stem cells shifted, and the homeostasis of the neurogenic niche was altered. Aging and neurodegenerative diseases reduced the phagocytic capacity of microglia, triggered astrogliosis, and altered the microvasculature of the dentate gyrus. Thus, enhanced vulnerability of AHN to neurodegeneration might underlie hippocampal dysfunction during physiological and pathological aging in humans.

The addition of new neurons to the hippocampus throughout life—a process known as adult hippocampal neurogenesis (AHN) (*1*, *2*)—boosts hippocampal plasticity. AHN also participates in mood regulation (*3*) and pattern separation (*4*). Although exhaustively studied in rodents (*1*) and Old World primates (*5*), this phenomenon has not been fully characterized in humans. The increased plasticity of the hippocampus serves as a double-edged sword, as this brain region also shows enhanced vulnerability to neurodegeneration. Although the hippocampus is not the most affected brain region, impairments in this structure are believed to underlie the cognitive decline and psychiatric symptoms observed in patients with various neurodegenerative diseases. Given the poorly characterized association between AHN and hippocampal dysfunction in humans, we sought to determine whether the dentate gyrus (DG) homeostasis and AHN dynamics show increased vulnerability to distinct forms of neurodegeneration.

AHN in neurologically healthy controls

To assess the presence of all elements encompassed by AHN throughout human life, we examined a cohort of neurologically healthy controls (Fig. 1 and figs. S1 to S7). Previous studies have identified immature dentate granule cells (DGCs) in the human DG (*6*–*9*); however, the presence of radial glia-like (RGL) cells with neural stem cell (NSC)

[1]Department of Molecular Neuropathology, Centro de Biología Molecular "Severo Ochoa" (CBMSO), Spanish Research Council (CSIC), Universidad Autónoma de Madrid (UAM), Madrid, Spain. [2]Department of Molecular Biology, Faculty of Sciences, Universidad Autónoma de Madrid, Madrid, Spain. [3]Center for Networked Biomedical Research on Neurodegenerative Diseases (CIBERNED), Madrid, Spain. [4]Laboratory of Neuronal Plasticity, Leloir Institute (IIBBA-CONICET), Buenos Aires, Argentina. [5]Faculty of Biomedical and Health Sciences, Universidad Europea de Madrid, Madrid, Spain. [6]Neuropathology Department, CIEN Foundation, Madrid, Spain.
*Corresponding author. Email: m.llorens@csic.es
†These authors contributed equally to this work.

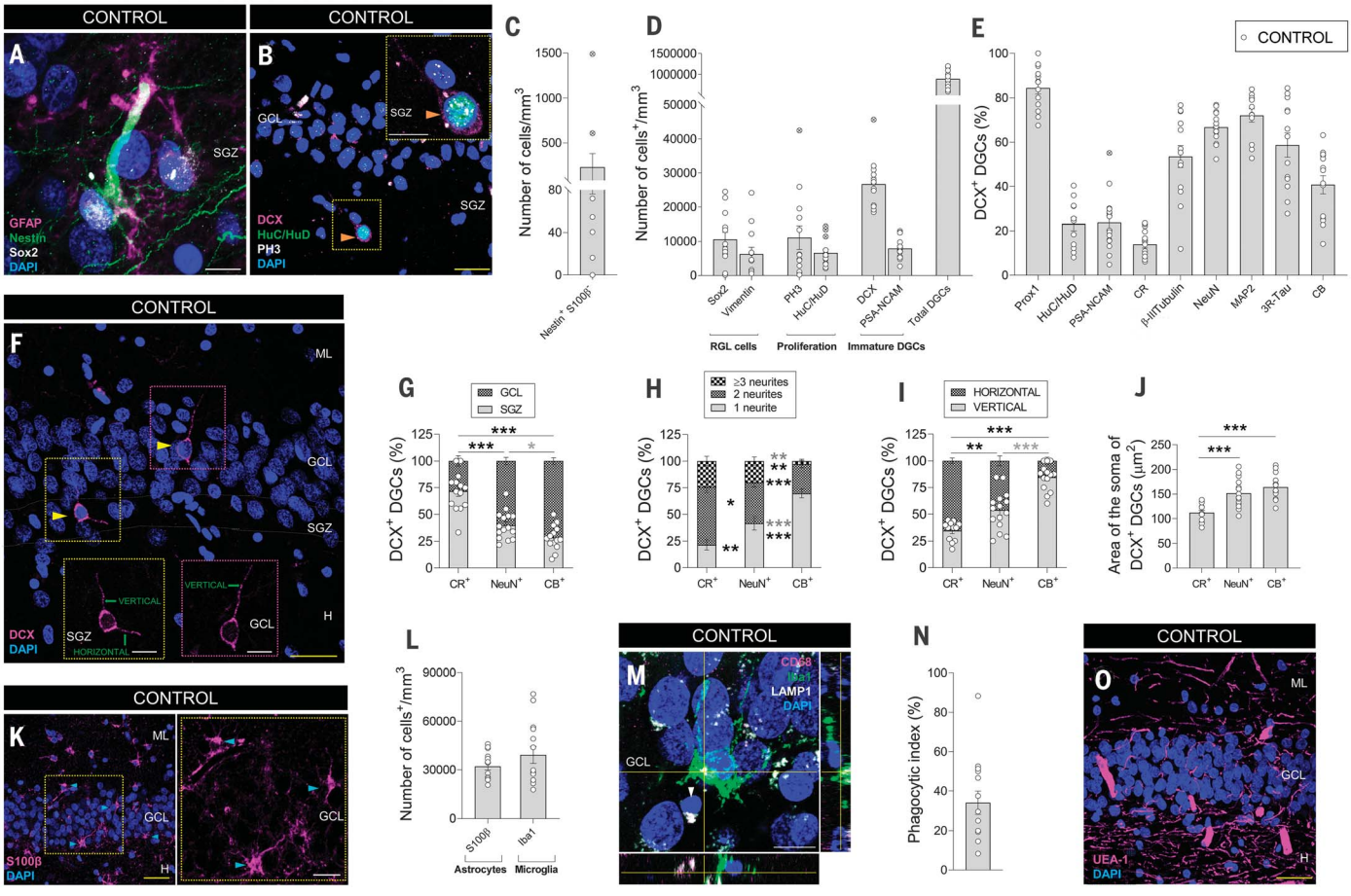

Fig. 1. Adult hippocampal neurogenesis in neurologically healthy controls. (**A** and **B**) Representative images of a nestin$^+$ SRY-box transcription factor 2 (Sox2)$^+$ glial fibrillary acidic protein (GFAP)$^+$ radial glia-like (RGL) cells (A), and a phospho-histone 3 (PH3)$^+$ HuC/HuD$^+$ doublecortin (DCX)$^+$ proliferative neuroblast (B) in the human dentate gyrus (DG). (**C** and **D**) Density of nestin$^+$ S100β$^-$ RGL cells (C), and Sox2$^+$, vimentin$^+$, PH3$^+$, Huc/HuD$^+$ cells, DCX$^+$, and polysialylated-neural cell adhesion molecule (PSA-NCAM)$^+$ immature and total dentate granule cells (DGCs) (D) in neurologically healthy controls. (**E**) Percentage of DCX$^+$ immature DGCs that express markers of distinct maturation stages. (**F**) Representative images showing morphologically undifferentiated (left) and differentiated (right) human DCX$^+$ immature DGCs. (**G**) Positioning of DCX$^+$ DGC subpopulations. (**H**) Number of primary neurites of DCX$^+$ DGCs. (**I**) Orientation of neurites in DCX$^+$ DGCs. (**J**) Area of the soma of DCX$^+$ DGCs. (**K**) Representative images of S100β$^+$ astrocytes. (**L**) Density of S100β$^+$ astrocytes and Iba1$^+$ microglia. (**M**) Representative image of an Iba1$^+$ microglial cell showing the presence of a phagocytic pouch in the proximity of a pyknotic nucleus in the human DG. (**N**) Phagocytic index. (**O**) Representative image showing the vascularization of the human DG. n = 15 neurologically healthy controls. In (A), (B), (F), (K), (M), and (O), Z-projection images are shown. For each marker, 5 to 20 stacks of images per subject were analyzed. Graphs represent mean values ± SEM. ML, molecular layer; GCL, granule cell layer; SGZ, subgranular zone; H, hilus; CR, calretinin; CB, calbindin; yellow scale bar, 50 μm; white scale bar, 10 μm; orange triangles, PH3$^+$ HuC/HuD$^+$ DCX$^+$ cells; yellow triangles, DCX$^+$ DGCs; blue triangles, S100β$^+$ astrocytes; white triangle, pyknotic nucleus. *0.05 > P ≥ 0.01; **0.01 > P ≥ 0.001; and ***P <0.001. Black asterisks indicate changes with respect to DCX$^+$ CR$^+$ DGCs. Gray asterisks indicate changes between DCX$^+$ NeuN$^+$ and DCX$^+$ CB$^+$ DGCs. Crossed-out dots in (C), (D), and (E) indicate outlier values.

properties (*10*) remains elusive. By subjecting high-quality postmortem human samples to state-of-the-art tissue preservation methodologies (*6*), we identified a population of nestin$^+$ cells that do not express S100β (Fig. 1C and fig. S3) but instead express other RGL markers, such as SRY-box 2 (Sox2), vimentin, and glial fibrillary acidic protein (GFAP) (Fig. 1, A and D). Unlike nestin$^+$ S100β$^+$ cells, nestin$^+$ S100β$^-$ RGL cells show the morphological characteristics of NSCs [e.g., the presence of long apical processes and predominant distribution of their cell bodies in the subgranular zone (SGZ)] (fig. S3). Phospho-histone 3 (PH3)$^+$ proliferative cells and HuC/HuD$^+$ proliferative neuroblasts were also detected in the SGZ (Fig. 1, B and D, and fig. S4). The presence of RGL and proliferative cells supports the notion that the human hippocampal NSC pool is preserved throughout life. These data agree with the identification of a cluster of human DGCs (by single-cell RNA sequencing), which are proposed to represent precursor granule cells with neurogenic capacity (*11*); these data are also compatible with the activation of quiescence mechanisms to maintain the proliferative capacity of NSCs and prevent their depletion (*12*).

Immature DGCs express the microtubule-associated protein doublecortin (DCX) and go through various differentiation stages before fully maturing (*7*) (fig. S2G). Although DCX and polysialylated neural cell adhesion molecule (PSA-NCAM) are considered equivalent as markers of immature neurons in the adult brain, the expression of the latter slightly precedes that of the former during human AHN (fig. S2, A to G). DCX is not expressed by astrocytes, microglia, vascular structures, or interneurons (fig. S5, A to F). By contrast, DCX$^+$ DGCs express Prox1 (Fig. 1E and fig. S2I) and other neuronal markers that characterize distinct DGC maturation stages (*7*), including proliferative neuroblasts (HuC/HuD), immature [PSA-NCAM, calretinin (CR), or β-III tubulin] and more differentiated DGCs [neuronal nuclei (NeuN), microtubule-associated protein 2 (MAP-2), three-repeat Tau (3R-Tau), and calbindin (CB) (Fig. 1E and figs. S2J and S4A). The expression of these markers varies during DGC maturation, and the cell positioning (Fig. 1, F and G), the presence (Fig. 1, F and H) and orientation (Fig. 1, F and I) of neurites, and the cell area (Fig. 1J and fig. S2H) are modified. In this regard, the most immature DCX$^+$ CR$^+$ DGCs are small, located in the SGZ, and have various primary apical neurites with horizontal orientation (*7*). By contrast, more differentiated DCX$^+$ CB$^+$ DGCs are larger, occupy upper positions in the granule cell layer (GCL) (fig. S2J), and have a single primary apical neurite oriented toward the molecular layer (*7*). Lastly, DCX$^+$ NeuN$^+$ DGCs show an intermediate state of maturation (Fig. 1, G to J, and fig. S2H), thereby supporting the dynamic nature of AHN in humans (fig. S2G).

In rodents, AHN is orchestrated by the astrocytes (*13*), microglia (*14*) and vasculature (*15*) of the DG neurogenic niche; however, the composition of a putatively equivalent structure in humans remains poorly characterized. We observed abundant astrocytes (Fig. 1, K and L) and microglia (Fig. 1, L to N), as well as a profuse network of *Ulex Europaea* agglutinin 1 (UEA-1)$^+$ capillaries that occupied ~7% of the human GCL surface (Fig. 1O and fig. S2L) and were located close to immature DGCs and RGL cells. Our observations reveal the cellular composition and remodeling of the human DG neurogenic niche throughout aging. Among the distinct components of this niche, microglia regulate AHN by controlling newborn neuron maturation (*14*). The former cells exhibit specialized membranous structures called phagocytic pouches, which allow them to engulf dysfunctional cells (*14*) (Fig. 1, M and N). The presence of such structures defines distinct morphological phenotypes in human microglia (fig. S6) and determines their phagocytic capacity (phagocytic index in mice) (Fig. 1N and fig. S6F) (*14*). This suggests that they may have similar functions in humans. Microglia lacking phagocytic pouches had long nonpolarized processes. By contrast, the presence of these structures is accompanied by polarized morphologies and profusely branched processes. We observed a reduced number of phagocytic pouches in aged participants (fig. S2M), thus pointing to a partially dysfunctional microglial phenotype and suggesting that altered microglial function is one of the mechanisms underpinning age-associated AHN decline in humans.

AHN in neurodegenerative diseases

Given the reduction of AHN during physiological aging, we questioned whether this phenomenon was also compromised by distinct forms of neurodegeneration. AHN was found to be altered in mouse models of amyotrophic lateral sclerosis (ALS) (*16*). In light of the hippocampal alterations (*17*) and increased density of pyknotic cells (fig. S8C) found in the DG of patients with ALS, we first assessed the vulnerability of AHN to this disorder (Fig. 2 and figs. S1 and S9). The densities of PH3$^+$ and HuC/HuD$^+$ cells remained unchanged (Fig. 2, C and E, and fig. S9A), thereby indicating that proliferation was preserved in these patients. By contrast, patients with ALS showed increased densities of NSCs (Fig. 2, A, B, D, and E) and DCX$^+$ immature DGCs (Fig. 2, F to I, and fig. S9, B to E), although the morphological development of the latter tended to be impaired (Fig. 2, I to K). Subsequently, we examined the integrity of the DG neurogenic niche and observed DG astrogliosis (Fig. 2, L and M) along with a reduced number of microglial phagocytic pouches (Fig. 2N). Moreover, DG capillaries tended to be thicker (Fig. 2P and fig. S9N). Taken together, these results indicate that both AHN and the homeostasis of the DG neurogenic niche are vulnerable to ALS. The AHN phenotype observed in these patients was characterized by increased numbers of RGL cells and immature DGCs that tended to be morphologically aberrant.

Hippocampal alterations (*18*) are believed to underlie the early spatial learning deficits observed in patients with Huntington's disease and are consistent with the presence of mutant huntingtin and the increased density of pyknotic nuclei observed in the DG of these patients (figs.

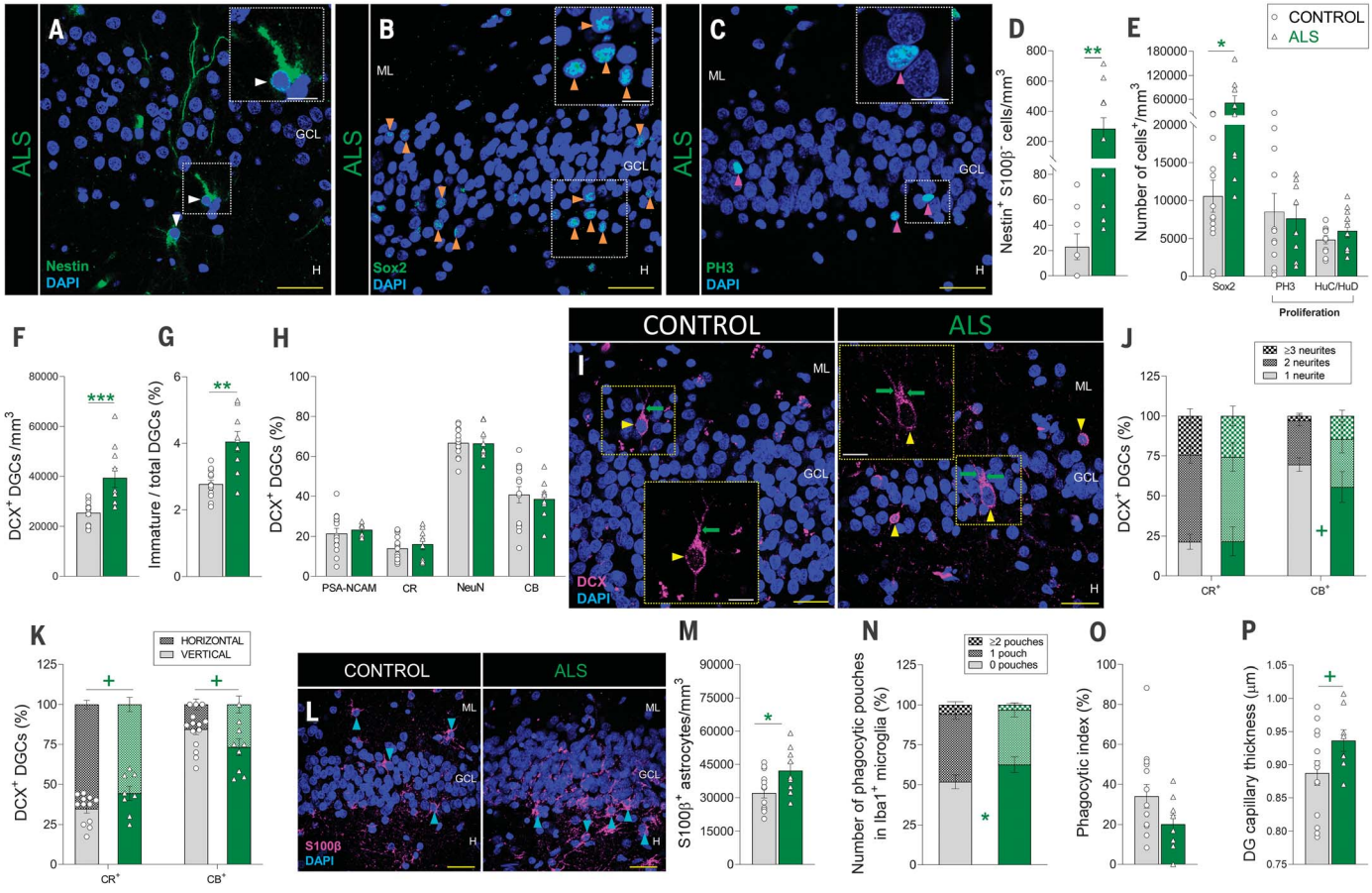

Fig. 2. Adult hippocampal neurogenesis in ALS. (**A** to **C**): Representative images of nestin$^+$ (A), Sox2$^+$ (B), and PH3$^+$ cells (C). (**D** and **E**) Density of nestin$^+$ S100β$^-$ RGL cells (D), Sox2$^+$ cells, PH3$^+$ proliferative cells, and HuC/HuD$^+$ proliferative neuroblasts (E). (**F**) Density of DCX$^+$ immature DGCs. (**G**) Ratio between immature and total DGCs. (**H**) Percentage of DCX$^+$ immature DGCs that express markers of distinct maturation stages. (**I**) Representative images of DCX$^+$ immature DGCs showing the presence of apical dendrites (green arrows). (**J**) Number of primary neurites in DCX$^+$ DGCs. (**K**) Orientation of primary neurites in DCX$^+$ DGCs. (**L**) Representative images of S100β$^+$ astrocytes. (**M**) Density of S100β$^+$ astrocytes. (**N**) Number of phagocytic pouches in Iba1$^+$ microglia. (**O**) Phagocytic index. (**P**) Thickness of *Ulex Europaea* agglutinin 1 (UEA-1)$^+$ DG capillaries. n = 15 neurologically healthy controls and 12 patients with ALS. In (A) to (C), (I), and (L), Z-projection images are shown. For each marker, 5 to 20 stacks of images per subject were analyzed. Graphs represent mean values ± SEM. ML, molecular layer; GCL, granule cell layer; SGZ, subgranular zone; H, hilus; CR, calretinin; CB, calbindin; yellow scale bar, 50 μm; white scale bar, 10 μm; white triangles, nestin$^+$ RGL cells; orange triangles, Sox2$^+$ cells; magenta triangles, PH3$^+$ cells; yellow triangles, DCX$^+$ DGCs; blue triangles, S100β$^+$ astrocytes. $^+0.1 > P \geq 0.05$; $^*0.05 > P \geq 0.01$; $^{**}0.01 > P \geq 0.001$; and $^{***}P < 0.001$. Green asterisks indicate changes with respect to neurologically healthy controls.

S10N and S8D). Therefore, we studied the targeting of AHN by Huntington's disease (Fig. 3 and figs. S1 and S10). The densities of nestin$^+$ S100β$^-$ NSCs (Fig. 3, A and D) and immature DGCs (Fig. 3, F and G) were increased in patients with this disorder, whereas those of Sox2$^+$ and proliferative cells (Fig. 3, B, C, and E) remained unchanged. Immature DGCs showed early maturation impairments (Fig. 3H), possibly related to their lengthened initial differentiation stages (Fig. 3I and fig. S10, L and M), morphological abnormalities (Fig. 3, L to N, and fig. S10, B and C), and reduced NeuN expression (Fig. 3H), which agrees with the AHN impairments observed in mouse models (*19*). The homeostasis of the DG neurogenic niche was also affected (Fig. 3, O to S, and fig. S10, F to K), as suggested by the presence of DG astrogliosis (Fig. 3O), microglial alterations [reduction in phagocytic index, number of phagocytic pouches (Fig. 3, P to R), and nucleus area (fig. S10I)] and increased capillary thickness (Fig. 3S and fig. S10K). These results reveal the vulnerability of AHN and DG homeostasis to Huntington's disease. In patients with the latter condition, newborn DGCs showed early and late maturation impairments that led to their retention at undifferentiated stages.

α-Synucleinopathies are characterized by the accumulation of α-synuclein aggregates in the brain. This family of disorders presents diverse clinical manifestations, including a variable temporal sequence of cognitive and motor impairments (*20*). We examined the integrity of AHN in two of these disorders, specifically Parkinson's disease (PD) and dementia with Lewy bodies (LD) (Fig. 4 and figs. S1, S11, and S12). Patients with these diseases showed an increased density of RGL cells (Fig. 4, A, B, E, and F) and morphological abnormalities in DCX$^+$ DGCs (Fig. 4, L and M, and figs. S11, E and F). However, other aspects of AHN seemed to be differentially altered in both conditions. Patients with PD showed increased densities of HuC/HuD$^+$ proliferative neuroblasts and DCX$^+$ immature DGCs (data S1), which presented reduced expression of NeuN (data S1). We observed increased densities of pyknotic cells (fig. S8E), compromised microglial phagocytic capacity (reduced phagocytic index and nucleus area)

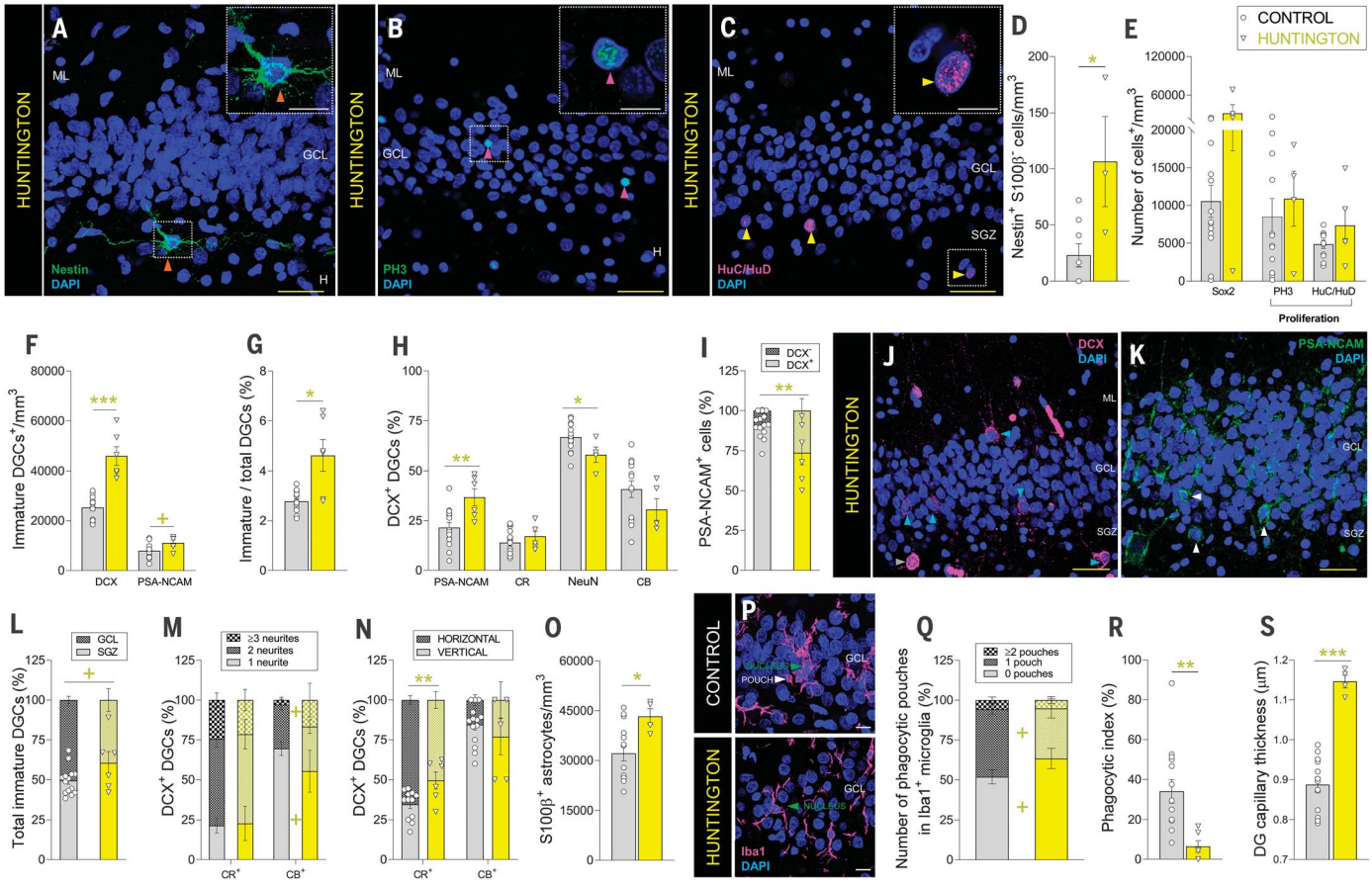

Fig. 3. Adult hippocampal neurogenesis in patients with Huntington's disease. (**A** to **C**) Representative images of nestin$^+$ cells (A), PH3$^+$ proliferative cells (B), and HuC/HuD$^+$ proliferative neuroblasts (C). (**D** to **E**) Density of nestin$^+$ S100β$^-$ RGL cells (D), Sox2$^+$ cells, PH3$^+$ proliferative cells, and HuC/HuD$^+$ proliferative neuroblasts (E). (**F**) Density of DCX$^+$ and Polysialylated-neural cell adhesion molecule (PSA-NCAM)$^+$ immature DGCs. (**G**) Ratio of immature to total DGCs. (**H**) Percentage of DCX$^+$ immature DGCs that express markers of distinct maturation stages. (**I**) Percentage of PSA-NCAM$^+$ DGCs that express DCX. (**J** to **K**) Representative images of DCX$^+$ (J) and PSA-NCAM$^+$ (K) immature DGCs. (**L**) Positioning of immature DGCs. (**M**) Number of primary neurites of distinct subpopulations of DCX$^+$ DGCs. (**N**) Orientation of neurites in DCX$^+$ DGCs. (**O**) Density of S100β$^+$ astrocytes. (**P**) Representative images of Iba1$^+$ microglia. (**Q**) Number of phagocytic pouches in Iba1$^+$ microglia. (**R**) Phagocytic index. (**S**) Thickness of UEA1$^+$ DG capillaries. n = 15 neurologically healthy controls and 6 patients with Huntington's disease. In (A) to (C), (J) to (K), and (P), Z-projection images are shown. For each marker, 5 to 20 stacks of images per subject were analyzed. Graphs represent mean values ± SEM. ML, molecular layer; GCL, granule cell layer; SGZ, subgranular zone; H, hilus; CR, calretinin; CB, calbindin; yellow scale bar, 50 μm; white scale bar, 10 μm; orange triangles, nestin$^+$ RGL cells; magenta triangles, PH3$^+$ cells; yellow triangles, HuC/HuD$^+$ cells; blue triangles, DCX$^+$ immature DGCs; white triangles, PSA-NCAM$^+$ immature DGCs. $^+0.1 > P \geq 0.05$; $^*0.05 > P \geq 0.01$; $^{**}0.01 > P \geq 0.001$; and $^{***}P < 0.001$. Yellow asterisks indicate changes with respect to neurologically healthy controls.

(Fig. 4, O to Q), and increased DG capillary thickness (Fig. 4, R and S, and fig. S11M) in both α-synucleinopathies. Patients with PD also presented DG astrogliosis, which indicates a more severe alteration in the integrity of the DG neurogenic niche (data S1). Collectively, these results reveal that these two α-synucleinopathies differentially target the DG milieu and generate singular AHN signatures (data S1). Although patients with PD presented a generalized increase in several neurogenic cell populations, which also showed maturation impairments, those with LD showed milder alterations in all of the aforementioned stages of AHN and the DG neurogenic niche.

In line with the diffuse degeneration of the frontal and temporal lobes of the brain (*21*), patients with frontotemporal dementia (FTD) also showed mild AHN alterations (Fig. 5 and figs. S1 and S13). They presented unchanged densities of NSCs (Fig. 5, C and D, and fig. S13, A and B) and immature DGCs (Fig. 5E and fig. S13, C to E), reduced densities of HuC/HuD$^+$ proliferative neuroblasts (Fig. 5, B and D), and moderately impaired DGC differentiation (Fig. 5, F to J, and fig. S13F). Mild signs of disturbed DG homeostasis (Fig. 5, K to O), such as increased density of pyknotic cells (fig. S8F), astrogliosis (Fig. 5, K and L), increased capillary thickness (Fig. 5O and fig. S13O), and a trend of reduced microglial phagocytic index (Fig. 5, M and N), were also observed. These results reveal that FTD moderately targets AHN by causing an imbalance in the ratio of RGL cells to proliferative cells, triggering the presence of morphologically aberrant DGCs, and altering the DG neurogenic niche homeostasis.

Our data reveal the vulnerability of human AHN to distinct neurodegenerative diseases. The heterogeneous nature of the hippocampal alterations in patients with ALS (*22*), Huntington's disease (*23*), α-synucleinopathies (*20*, *24*), or FTD (*21*) is likely to underlie the specific disease-associated AHN signatures

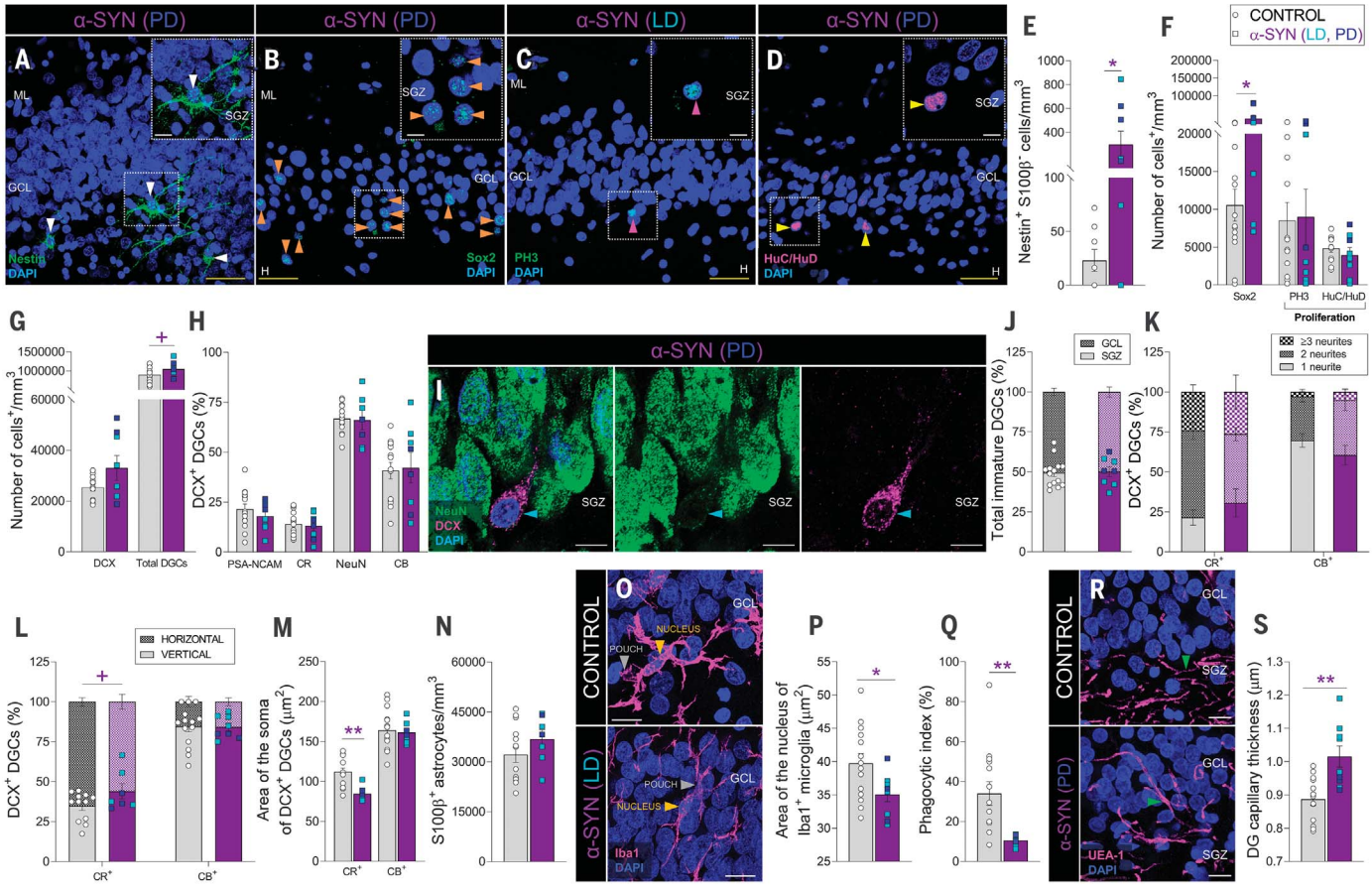

Fig. 4. Adult hippocampal neurogenesis in participants with α-synucleinopathies (α-SYN). (**A** to **D**) Representative images of nestin$^+$ (A), Sox2$^+$ (B), PH3$^+$ cells (C), and HuC/HuD$^+$ proliferative neuroblasts (D). (**E** to **F**) Density of nestin$^+$ S100β$^-$ RGL cells (E), Sox2$^+$ cells, PH3$^+$ proliferative cells, and HuC/HuD$^+$ proliferative neuroblasts (F). (**G**) Density of DCX$^+$ and total DGCs. (**H**) Percentage of DCX$^+$ immature DGCs that express markers of distinct maturation stages. (**I**) Representative high-power magnification images of a DCX$^+$ DGC. (**J**) Positioning of immature DGCs. (**K**) Number of primary neurites of distinct subpopulations of DCX$^+$ DGCs. (**L**) Neurite orientation in DCX$^+$ DGCs. (**M**) Area of the soma of DCX$^+$ DGCs. (**N**) Density of S100β$^+$ astrocytes. (**O**) Representative images of Iba1$^+$ microglia. (**P**) Area of the nucleus of Iba1$^+$ microglia. (**Q**) Phagocytic index. (**R**) Representative images showing the vascularization of the dentate gyrus (DG). (**S**) Thickness of UEA-1$^+$ DG capillaries. n = 15 neurologically healthy controls and 9 patients with α-SYN [3 with Parkinson's disease (PD) and 6 with dementia with Lewy bodies (LD)]. In (A) to (D), (I), (O), and (R), Z-projection images are shown. For each marker, 5 to 20 stacks of images per subject were analyzed. Graphs represent mean values ± SEM. ML, molecular layer; GCL, granule cell layer; SGZ, subgranular zone; H, hilus; CR, calretinin; CB, calbindin; yellow scale bar, 50 μm; white scale bar, 10 μm; white triangles, nestin$^+$ RGL cells; orange triangles, Sox2$^+$ cells; magenta triangles, PH3$^+$ cells; yellow triangles, HuC/HuD$^+$ cells; blue triangles, DCX$^+$ immature DGCs; green triangles, UEA1$^+$ capillaries. $^+0.1 > P \geq 0.05$; * $0.05 > P \geq 0.01$; ** $0.01 > P \geq 0.001$; and ***$P < 0.001$. Purple asterisks indicate changes with respect to neurologically healthy controls.

observed (Fig. 6 and data S1). The imbalanced number of RGL and proliferative cells noted in patients with ALS, Huntington's disease, LD, and FTD point to enhanced quiescence of the former cells or to impaired survival of their immediate progeny, thus suggesting selective vulnerability of RGL and proliferative cells to certain disorders. By contrast, other aspects of AHN, such as DGC maturation, were affected in all the diseases studied and might be caused by the global disruption of DG homeostasis. In addition to local pathological effects, the neurodegeneration of other brain areas primarily affected by these conditions might alter the DG homeostasis through long-distance signaling mechanisms. In this regard, the observed increase in DG vascularization might either exert neuroprotective effects or amplify the detrimental consequences of local and distal neuroinflammation, thereby contributing to the progressive impairment of microglial functions. The reduction of microglial phagocytic capacity correlates with the number of DG pyknotic cells and the severity of AHN impairments in patients with ALS, Huntington's disease, and α-synucleinopathies. Moreover, impaired microglial phagocytosis triggers astrogliosis (*25*), a phenomenon evident in all diseased individuals examined in this study. Therefore, the generalized alteration of DG homeostasis might be a direct pathway through which neurodegenerative diseases target AHN dynamics in humans.

AHN is crucial in learning, memory, and mood regulation; in fact, failure of AHN is related to memory deficits in humans (*8*, *26*). Our results point to AHN impairment as a mechanism underlying hippocampal dysfunction in aged and diseased patients. Unraveling the complex cross-talk established between the elements that make up the human DG neurogenic niche and AHN dynamics is expected to improve our understanding of the physiological roles played by AHN, which

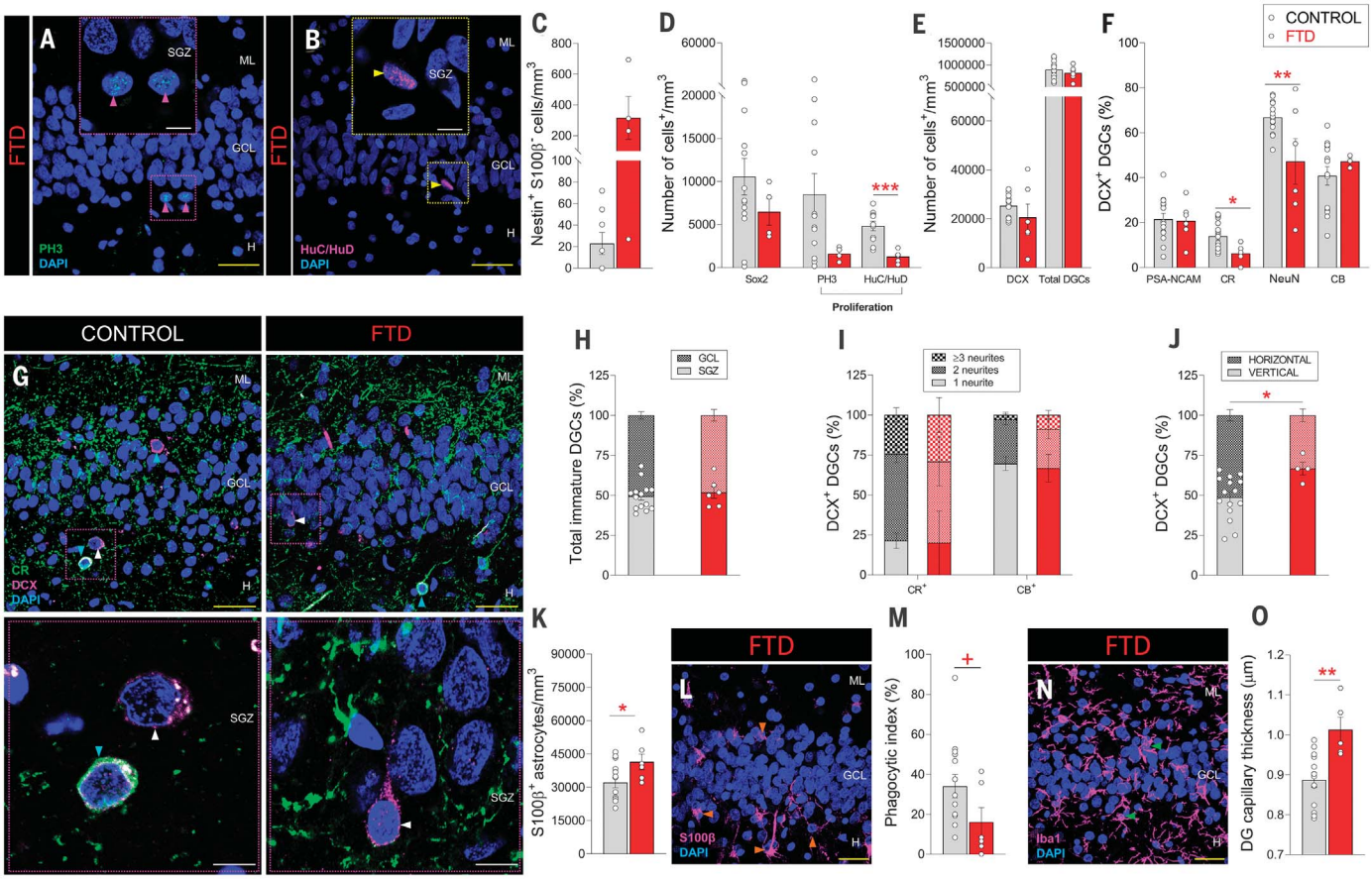

Fig. 5. Adult hippocampal neurogenesis in frontotemporal dementia (FTD). (**A** to **B**) Representative images of PH3$^+$ proliferative cells (A) and HuC/HuD$^+$ proliferative neuroblasts (B) in patients with FTD. (**C to D**) Density of nestin$^+$ S100β$^-$ RGL cells (C), Sox2$^+$ cells, PH3$^+$ proliferative cells, and HuC/HuD$^+$ proliferative neuroblasts (D). (**E**) Density of DCX$^+$ and total DGCs. (**F**) Percentage of DCX$^+$ immature DGCs that express markers of distinct maturation stages. (**G**) Representative low- and high-power magnification images of DCX$^+$ DGCs. (**H**) Positioning of total immature DGCs. (**I**) Number of neurites in DCX$^+$ DGCs. (**J**) Neurite orientation in DCX$^+$ DGCs. (**K**) Density of S100β$^+$ astrocytes. (**L**) Representative images of S100β$^+$ astrocytes. (**M**) Phagocytic index. (**N**) Representative images of Iba1$^+$ microglia. (**O**) Thickness of UEA-1$^+$ dentate gyrus capillaries. n = 15 neurologically healthy control patients and 6 patients with FTD. In (A), (B), (G), (L), and (N), Z-projection images are shown. For each marker, 5 to 20 stacks of images per subject were analyzed. Graphs represent mean values ± SEM. ML, molecular layer; GCL, granule cell layer; SGZ, subgranular zone; H, hilus; CR, calretinin; CB, calbindin; yellow scale bar, 50 μm; white scale bar, 10 μm; magenta triangles, PH3$^+$ cells; yellow triangles, HuC/HuD$^+$ cells; blue triangles, DCX$^+$ CR$^+$ immature DGCs; white triangles, DCX$^+$ CR$^-$ immature DGCs; orange triangles, S100β$^+$ astrocytes; green triangles, Iba1$^+$ microglia. $^+0.1 > P \geq 0.05$; * $0.05 > P \geq 0.01$; ** $0.01 > P \geq 0.001$; and ***$P < 0.001$. Red asterisks indicate changes with respect to neurologically healthy controls.

functions as a lifelong reserve of plasticity in the human brain.

REFERENCES AND NOTES

1. J. Altman, *Anat. Rec.* **145**, 573–591 (1963).
2. P. S. Eriksson *et al.*, *Nat. Med.* **4**, 1313–1317 (1998).
3. A. S. Hill, A. Sahay, R. Hen, *Neuropsychopharmacology* **40**, 2368–2378 (2015).
4. A. Sahay *et al.*, *Nature* **472**, 466–470 (2011).
5. E. Gould *et al.*, *Proc. Natl. Acad. Sci. U.S.A.* **96**, 5263–5267 (1999).
6. M. Flor-García *et al.*, *Nat. Protoc.* **15**, 668–693 (2020).
7. E. P. Moreno-Jiménez *et al.*, *Nat. Med.* **25**, 554–560 (2019).
8. M. K. Tobin *et al.*, *Cell Stem Cell* **24**, 974–982.e3 (2019).
9. M. Boldrini *et al.*, *Cell Stem Cell* **22**, 589–599.e5 (2018).
10. B. Seri, J. M. García-Verdugo, B. S. McEwen, A. Alvarez-Buylla, *J. Neurosci.* **21**, 7153–7160 (2001).
11. F. Ayhan *et al.*, *Neuron* **109**, 2091–2105.e6 (2021).
12. L. Harris *et al.*, *Cell Stem Cell* **28**, 863–876.e6 (2021).
13. S. Sultan *et al.*, *Neuron* **88**, 957–972 (2015).
14. A. Sierra *et al.*, *Cell Stem Cell* **7**, 483–495 (2010).
15. T. D. Palmer, A. R. Willhoite, F. H. Gage, *J. Comp. Neurol.* **425**, 479–494 (2000).
16. Z. Liu, L. J. Martin, *J. Comp. Neurol.* **497**, 468–488 (2006).
17. F. Christidi *et al.*, *Neurobiol. Aging* **84**, 178–188 (2019).
18. K. L. Harris *et al.*, *Cortex* **119**, 417–427 (2019).
19. J. Terreros-Roncal *et al.*, *J. Neurosci.* **39**, 5794–5815 (2019).
20. L. Walker, L. Stefanis, J. Attems, *J. Neurochem.* **150**, 467–474 (2019).
21. M. Bocchetta *et al.*, *J. Alzheimers Dis.* **64**, 497–504 (2018).
22. S. Abdulla *et al.*, *Neurobiol. Aging* **35**, 2639–2645 (2014).
23. M. A. Curtis *et al.*, *Proc. Natl. Acad. Sci. U.S.A.* **100**, 9023–9027 (2003).
24. G. U. Höglinger *et al.*, *Nat. Neurosci.* **7**, 726–735 (2004).
25. H. Konishi *et al.*, *EMBO J.* **39**, e104464 (2020).
26. J. K. Young, *J. Alzheimers Dis. Rep.* **4**, 365–371 (2020).

ACKNOWLEDGMENTS

The authors thank the participants and their families for donating brain samples. They also thank I. Rodal, E. Hitt, and L. Saiz for their help with human sample extraction and processing; the Confocal Microscopy Facility at the CBMSO for their technical assistance; B. Berninger and B. Márquez-Valadez for their critical discussion of the data and help with manuscript preparation; and E. Terreros for support with designing the Excel macros. A number of human samples were provided by the Biobanco del Hospital Universitario Reina Sofía (Córdoba, Spain). The authors thank R. Sánchez for providing some of these samples. Requests for the prospective collection of equivalent brain samples will be fulfilled by A.R. under a material transfer agreement with the CIEN Foundation.

Funding: M.L.L.-M. was supported by the European Research Council (ERC) (ERC-CoG-2020-101001916), Spain's Ministry of Economy and Competitiveness (PID2020-113007RB-I00, SAF-2017-82185-R, and RYC-2015-171899), the Alzheimer's Association (2015-NIRG-340709, AARG-17-528125, and AARG-17-528125-RAPID), the Association for Frontotemporal Degeneration (2016 Basic Science Pilot Grant Award), and the Center for Networked Biomedical Research on Neurodegenerative Diseases (CIBERNED, Spain). Institutional grants from the Fundación Ramón Areces and Banco de Santander to CBMSO. are also acknowledged. The salary of J.T.-R. was supported by a doctoral fellowship from the Universidad Autónoma de Madrid (FPI-UAM 2017 program). The salary of E.P.M.-J. was supported by a 2018 Neuroscience doctoral fellowship from the Fundación Tatiana Pérez de Guzmán. The salary of M.F.-G. was supported by a Formación de Personal Investigador (FPI) contract, associated with the SAF-2017-82185-R grant (M.L.L.-M.) and supported by the Spain's Ministry for Economy and Competitiveness (PRE2018-085233). The salary of C.B.R.-M. is supported by "Subvenciones para la promoción de

A

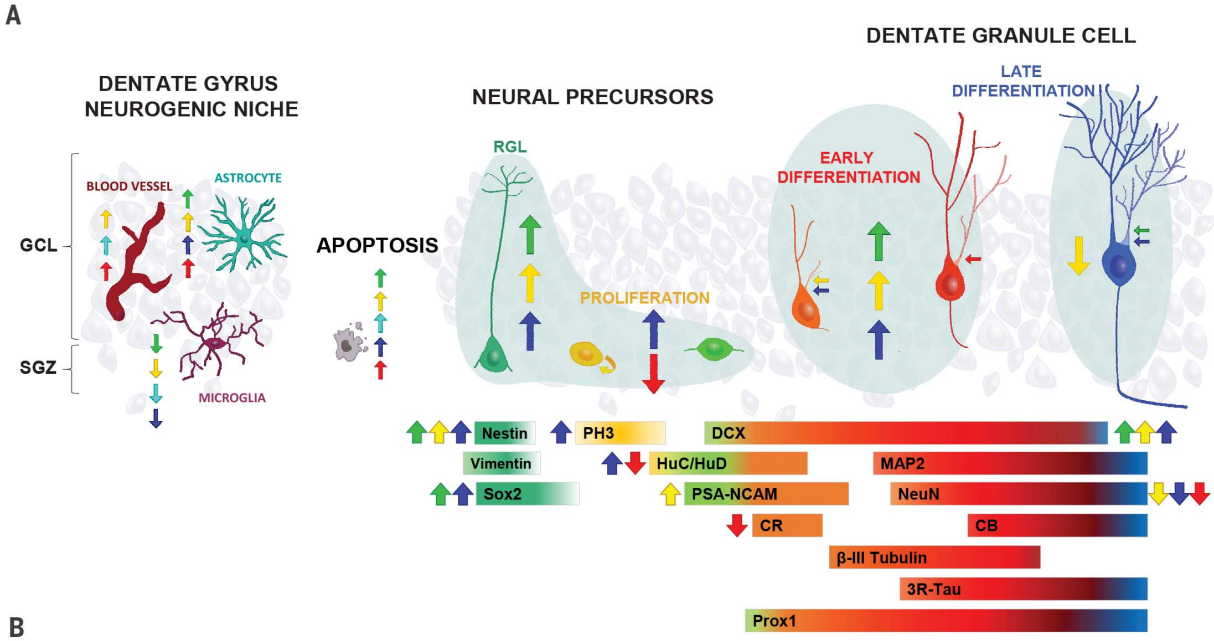

B

			α- SYNUCLEOINOPATHIES		
	ALS	HUNTINGTON	LEWY	PARKINSON	FTD
DENTATE GYRUS NEUROGENIC NICHE					
Astrocytes	↑	↑	=	↑	↑
Microglia	↓ Phagocytic pouches	↓ *Phagocytic index*	↓ Nucleus size ↓ *Phagocytic index*	↓ Phagocytic pouches	=
Vasculature	=	↑	↑	=	↑
APOPTOSIS					
Pyknotic cells	↑	↑	↑	↑	↑
NEURAL PRECURSORS					
RGL cells	↑	↑	=	↑	=
Proliferation	=	=	=	↑	↓
DENTATE GRANULE CELLS					
Immature DGCs	↑	↑	=	↑	=
Morphological maturation	Tendency to be altered	Altered	Altered	Altered	Altered
Differentiation (marker expression)	=	Altered	=	Altered	Altered
Total DGCS	=	↑	=	=	=

Fig. 6. Adult hippocampal neurogenesis (AHN) in neurodegenerative diseases. (**A**) Graphical scheme showing the stages of AHN targeted by each neurodegenerative disease. (**B**) Summary of the main alterations found in each disease.

empleo joven e Implantación de la garantía juvenil en I+D+i 2018" (PEJ2018-001725-A), awarded by Spain's Ministry of Economy and Competitiveness to M.L.L.-M. **Author contributions:** Conceptualization: J.T.-R., E.P.M.-J., M.F.-G., A.R., and M.L.L.-M. Data curation: J.T.-R. and M.L.L.-M. Formal Analysis: J.T.-R., E.P.M.-J., M.F.-G., C.B.R.-M., F.C., and M.L.L.-M. Funding acquisition: M.L.L.-M. Investigation: J.T.-R., E.P.M.-J., M.F.-G., C.B.R.-M., A.R., F.C., and M.L.L.-M. Methodology: J.T.-R., E.P.M.-J., M.F.-G., C.B.R.-M., A.R., and M.L.L.-M. Project administration: M.L.L.-M. Resources: A.R. and L.L.M. Supervision: M.L.L.-M. Validation: J.T.-R., E.P.M.-J., M.F.-G., A.R., and M.L.L.-M. Visualization: J.T.-R., E.P.M.-J., M.F.-G., A.R., and M.L.L.-M. Writing – original draft: M.L.L.-M. Writing – review and editing: J.T.-R., E.P.M.-J., M.F.-G., C.B.R.-M., A.R., M.F.T., F.C., and M.L.L.-M. **Competing interests:** Authors declare no competing interests. **Data and materials availability:** All data are available in the main text or the supplementary materials.

SUPPLEMENTARY MATERIALS

science.org/doi/10.1126/science.abl5163
Materials and Methods
Figs. S1 to S17
Tables S1 to S3
References (*27*–*34*)
MDAR Reproducibility Checklist
Data S1 and S2

View/request a protocol for this paper from Bio-protocol.

19 July 2021; accepted 6 October 2021
Published online 21 October 2021
10.1126/science.abl5163

Science

Impact of neurodegenerative diseases on human adult hippocampal neurogenesis

J. Terreros-RoncalE. P. Moreno-JiménezM. Flor-GarcíaC. B. Rodríguez-MorenoM. F. TrincheroF. CafiniA. RábanoM. Llorens-Martín

Science, 374 (6571), • DOI: 10.1126/science.abl5163

Disease and hippocampal dysfunction

Impaired function of the brain's hippocampus can underpin psychiatric symptoms and cognitive impairment. Looking at postmortem brain samples from patients affected by any of several neurodegenerative disorders, Terreros-Roncal *et al*. investigated whether adult neurogenesis was disrupted (see the Perspective by Gage). Indeed, functions of the neurogenic niche shifted and the cells produced were abnormal in shape and differentiation. The neuronal plasticity characteristic of the hippocampus may make it especially susceptible to the ravages of neurodegenerative disease. — PJH

Science (ISSN) is published by the American Association for the Advancement of Science. 1200 New York Avenue NW, Washington, DC 20005. The title *Science* is a registered trademark of AAAS.